High-pressure behavior of P2/n omphacite

High-pressure behavior of *P*2/*n* omphacite

FRANCESCO PANDOLFO[1,*], FABRIZIO NESTOLA[2], FERNANDO CÁMARA[3], M. CHIARA DOMENEGHETTI[1]

[1]Dipartimento di Scienze della Terra, Università di Pavia, via Ferrata 1, I-27100 Pavia, Italy

[2]Dipartimento di Geoscienze, Università di Padova, via Giotto 1, I-35137 Padova, Italy

[3]Dipartimento di Scienze Mineralogiche e Petrologiche, Università degli Studi di Torino, via Valperga Caluso 25, I-10125 Torino, Italy

*E-mail: francesco.pandolfo@unipv.it

ABSTRACT

High-pressure and room-temperature single-crystal X-ray diffraction (XRD) study has been performed using diamond-anvil cell on a crystal of *P*2/*n* natural omphacite sample with composition very close to $Jd_{52}Ag_{48}$ and with high degree of order in the cation distribution. Unit-cell parameters were determined at 13 different pressures up to about 7.5 GPa. A third-order Birch-Murnaghan equation of state (BM3-EoS) fit to the *P*-*V* data yielded V_0 = 421.43(4) Å^3, K_{T0} =122(1) GPa and K' =5.1(3). The K_{T0} value for this sample lies between the data obtained for the two end-members jadeite and diopside, describing a slight positive curvature trend.

During the same experiment, intensity data were collected and crystal structures were refined at 5 pressures up to 7.3 GPa. Both M1 and M2 polyhedra volumes showed a slight but significant change in slope at about 4 GPa. Such behavior cannot be explained in terms of bond lengths compression anomaly but much likely in terms of tilt angle variation of TA and TB tetrahedral, which also showed a change in slope with pressure.

Keywords: pyroxene, omphacite, high-pressure, single crystal XRD, crystal structures, diamond-anvil cell, Equation of State.

INTRODUCTION

Several recent X-ray diffraction studies have been focused on the behavior under high-pressure conditions of clinopyroxene with different compositions (Downs 2003; Origlieri et al. 2003; Thompson et al. 2005; Bindi et al. 2006; McCarty et al. 2008; Nestola et al. 2005, 2006, 2007, 2008a, 2010; Gavrilenko et al. 2010). Such large number of investigations is likely due to the very wide range of geological high-pressure environments in which this mineral is found, from methamorphic rocks to meteorites and also as inclusions in diamonds (e.g. Nestola et al. 2007; Koch-Mueller et al. 2004). In particular, clinopyroxenes are significantly abundant in the upper mantle, and most mineralogical and geophysical investigations have been concentrated on shedding light on the extremely complex geodynamic processes occurring at that depth (e.g. Agee 1999). The knowledge of the compressional and thermal behavior of clinopyroxenes is fundamental for understanding the geological environments in which these silicates play a crucial role. Concerning the high-pressure behavior of Na-clinopyroxene, X-ray diffraction studies have been performed both on jadeite, aegirine, hedenbergite end-members and on jadeite - aegirine and jadeite – hedenbergite solid solutions (Nestola et al. 2006; Nestola et al. 2007; Nestola et al. 2008a). The compressional behavior of omphacite (solid solution between $CaMgSi_2O_6$, Di – $NaAlSi_2O_6$, Jd, end-members) was investigated for the disordered phase with *C*2/*c* space group by McCormick et al. (1989) by single-crystal X-ray diffraction and by Nishihara et al. (2003) using an in situ multi anvil apparatus by X-ray synchrotron radiation; for the ordered phase, with *P*2/*n* space group, it was studied by Pavese et al. (2001) on powder material by X-ray synchrotron radiation. However no studies on the structural behavior at high pressure have been performed so far on this mineral. The aim of this work is to define for the first time the crystal structure evolution as a function of pressure and the pressure – volume equation of state for a natural ordered omphacite *P*2/*n* with low Fe content by single-crystal X-ray diffraction (SCXRD).This work is part of a wider project focused on the high-pressure and high-temperature behavior of natural and synthetic Na-bearing pyroxenes.

Key-words: omphacite, high-pressure, single-crystal, X-ray, diffraction

EXPERIMENTAL METHODS

Sample

The sample investigated at high-pressure in this work comes from the same crystal suite studied by Boffa Ballaran et al. (1998) and in particular it is labeled as their sample 74AM33. The chemical analysis of this sample is reported in Table 1. The sample has been selected for its very low Fe content in order to avoid the effect of iron on the Di-Jd solid solution. This sample also presents the highest degree of order for a natural omphacite among the samples studied by Boffa Ballaran et al. (1998). From this sample we picked up a single crystal, labeled as N.4, suitable for the high-pressure experiments due to its sharp optical extinction, sharp diffraction profiles, absence of twinning and evident defects and appropriate crystal size (0.17 x 0.12 x 0.05 mm).

Chemistry

Chemical analysis was performed on the same crystal used for the high-pressure work. After extracting crystal from the DAC it was embedded in epoxy resin and polished for electron microprobe analysis (EMPA), which were carried out at the Dipartimento di Geoscienze (University of Padova) using a CAMECA-CAMEBAX electron microprobe operating in wavelength dispersive mode with a fine-focused beam (~1 mm diameter), an acceleration voltage of 20 kV and a beam current of 10 nA, with 10 s counting times for both peak and total background. X-ray counts were converted to oxide wt.% using the PAP correction program supplied by CAMECA (Pochou and Pichoir, 1991). Standards, spectral lines, and analytical crystals used were: albite (Na-Ka, TAP), wollastonite (Si, Ca-Ka, TAP), olivine (Mg-Ka, TAP), Al_2O_3 (Al-Ka, TAP), $MnTiO_3$ (Mn-Ka, LiF; Ti- Ka, PET), Cr_2O_3 (Cr-Ka, LiF), Fe_2O_3 (Fe-Ka, LiF). The oxide wt.% obtained by averaging 15 microprobe analyses are reported in Table 1.

Single-crystal on air X-ray diffraction

The on air intensity data collection was collected at the University of Pavia on a three-circle Bruker AXS SMART APEX diffractometer, equipped with a CCD detector (graphite-monocrhromatized MoKα radiation λ=0.71073 Å, 55 kV, 30 mA) and a monocarp collimator. The Bruker SMART software package was used. A total of 3360 frames (frame resolution 512x512 pixels) were collected with four different goniometer settings using the ω-scan mode (scan width: 0.2 °ω; exposure time: 10 s; detector sample distance 4.02 cm). A total of 10337 reflections were collected. Completeness of the measured data was achieved up to 78° θ. The Bruker SAINT+ software was used for data reduction, including intensity integration and background and Lorentz-Polarization corrections. The semi-empirical absorption correction of Blessing (1995), based on the determination of transmission factors for equivalent reflections, was applied using the program SADABS (Sheldrick 1996) and the monoclinic Laue group 2/*m*. The intensity data were refined in the *P*2/*n* space group using program SHELX-97 (Sheldrick 2008) starting from the atom coordinates by (Pavese et al. 2000). Scattering curves were taken from the *International Tables for X-ray Crystallography* (Wilson 1995). Neutral versus ionized scattering factors were used to refine occupancy for all sites that are not involved in chemical substitutions (O and Si) (Hawthorne et al. 1995) and ionized scattering factors were used for cationic sites. When the refinement reached convergence, full-matrix least-squares were carried out using the data from the electron microprobe analysis (with 1 σ error) as chemical constraints to obtain the site partitioning. The following restraints were introduced into the refinement: (1) all structural sites were considered fully occupied; (2) Al^{3+} was distributed between T, M11 and M1; (3) Mn^{2+} was ordered in M1 while Cr and Ti were considered ordered in M11; (4) Fe^{2+} and Mg were considered as present in both M1 and M11, while Fe^{2+} only in M2 and Mg in M21; 5) charge balance was ensured by the equation $X_{Na}^{M2} + X_{Na}^{M21} = X_{Al3+} + X_{Al}^{M11} + X_{Al}^{M1} + 2X_{Ti} + X_{Cr}$; (6) additional equations based on the <M1-O> and <M11-O> observed mean bond distances were used to better constrain the site partitioning of Mg and Al in M1 and M11 sites. These equations are $\langle M1\text{-}O\rangle = 2.077Mg_{M1} + 1.928Al_{M1} + 2.130Fe^{2+}_{M1} + 2.173Mn_{M1}$ and $\langle M11\text{-}O\rangle = 2.077Mg_{M11} + 1.928Al_{M11} + 2.130Fe^{2+}_{M11} + 1.990Ti_{M11}$

+ 2.01Cr_{M11}. The values of mean bond distances for Mg, Al and Fe^{2+} are from Boffa Ballaran et al. (1998), values for Mn, Ti and Cr are from Zema et al. (1997). The mean atomic numbers calculated for the octahedral sites [$m.a.n._{M1+M11+M2+M21}$] by EMPA [28.87(13)] and by SCXRD [28.74(31)] are in agreement within their errors. The unit-cell parameters of the crystal in air are reported in Table 2, the values of the conventional agreement factor R1 as well as other details from the chemical constrained structure refinement are reported in Table 3. The site populations obtained from this refinement are reported in Table 4, fractional coordinates and displacement parameters in Table 5, bond lengths and angles in Table 6. The full structural data are also been deposited as cif[1].

Single-crystal High-pressure X-ray diffraction

The high-pressure SCXRD experiments were carried out at the Dipartimento di Geoscienze, Università di Padova. Crystal N.4 was loaded in an ETH-type DAC (Miletich et al. 2000) using a steel gasket (T301), pre-indented to a thickness of 110 μm and with a 250 μm diameter hole. A single crystal of quartz was used as internal diffraction pressure standard (Angel et al. 1997) and a 16:3:1 mixture of methanol:ethanol:water was used as hydrostatic pressure medium, which remains hydrostatic up to about 9.5-10 GPa (Angel et al. 2007). Unit-cell parameters were determined at 13 different pressures up to about 7.5 GPa using a STOE STADI-IV four-circle diffractometer (operating at 50 kV and 40 mA) automated by SINGLE software (Angel and Finger 2011). The unit-cell parameters were measured centering about 20 reflections for each high-pressure experiment. Full details of the instrument and the peak-centering algorithms are provided by Angel (2001). During the centering procedure the effects of crystal offsets and diffractometer aberrations were eliminated from refined peak positions by the eight-position centering method of King and Finger (1979). Unit-cell parameters, obtained by vector least-squares (Ralph and Finger 1982) are reported for each pressure step in Table 2. The intensity data were collected every about 2 GPa using a second STOE STADI-IV single-crystal diffractometer equipped with a CCD detector

131 located in the same Department (graphite monochromated Mo$K\alpha$ radiation, Oxford Diffraction).
132 The intensity data were collected in the $5 \leq 2\theta \leq 60°$ range using a 1° ω-scan and an exposure time
133 of 60 s per frame. The sample detector distance was 60 mm. The program CrysAlis RED (Oxford
134 Diffraction) was used to integrate the intensity data, applying the Lorentz-polarization correction.
135 ABSORB 6.0 (Angel 2004) program was adopted to correct for absorption and also take into
136 account the effect of gasket shadowing (Angel 2001). The package SHELX-97 (Sheldrick 2008)
137 was used for structure refinements, which were performed in space group *P*2/*n*, starting from the
138 atomic coordinates of Pavese et al. (2000). The atomic scattering curves were taken from the
139 *International Tables for X-ray Crystallography* (Wilson 1995). Isotropic displacement parameters
140 were considered for all atoms. For each high pressure refinement the site occupancies were
141 constrained to the values obtained from the on air refinement (see Table 4). The values of the
142 conventional agreement factor R_1 as well as other details from every pressure step refinement are
143 reported in Table 3. Fractional coordinates and displacement parameters are reported in Table 5,
144 bond lengths and angles in Table 6. The full structural data are also been deposited as cifs[1].
145
146 [1] Cif deposit items are available via the MSA web site at http://www.minsocam.org, go to the
147 American Mineralogist Contents, find the table of contents for the specific volume/issue wanted,
148 and then click on the deposit link there.
149
150 **RESULTS**
151 ***Order degree***
152 The site population (Table 4) was used to calculate the order parameters Q_{M1} and Q_{M2} of the M1
153 and M2 sites using equations (2) and (3) provided by Carpenter et al. (1990) expressed as Eqn. 1and
154 Eqn. 2 . They resulted to be: $Q^{occ}_{M1} = 0.896$ and $Q^{occ}_{M2} = 0.499$. These values are in agreement with
155 those reported by Boffa Ballaran (1998) for the same 74AM33 sample. The order parameters
156 expressed in terms of mean bond lengths were calculated using Eqn.3 and Eqn.4 provided by

Carpenter et al. (1990), which yielded: Q^{dist}_{M1} = 0.0689 and Q^{dist}_{M2} = 0.0161(Table 4). The correlation between the two parameters confirms the low aegirine content for N4 sample (see Fig. 2 by Carpenter et al. 1990).

Evolution of the unit-cell parameters with pressure and pressure – volume equation of state

The evolutions of the unit-cell parameters and unit-cell volume with pressure are shown in Figure 1a and 1b. A continuous decrease of *a*, *b*, *c*, β angle and volume, *V*, is observed as a function of pressure with no evidence of a phase transition up to the maximum pressure reached. The *a*, *b*, *c* lattice parameters decrease by about 1.8, 2.0 and 1.9% up to 7.5 GPa, respectively, β by 0.7% and the unit-cell volume decreases by about 5.2%.

In order to define the best equation of state that adequately describes the pressure-volume trend for the sample here studied an F_E-f_E plot was constructed following Angel (2001) and is shown in Figure 2. The plot shows that data lie on a positively inclined straight line indicating that a Birch-Murnaghan equation of state truncated at the third-order (BM3-EoS, Birch 1947) must be used to fit the experimental pressure-volume data. Thus, using EoS-FIT 5.2 software (Angel 2002) it was possible to refine simultaneously to a BM3 the volume, V_0, the bulk modulus K_{T0}, and its first pressure derivative K' obtaining the following coefficients: V_0 = 421.43(4) Å^3, K_{T0} = 122(1) GPa, K' = 5.1(3). The quality of the experimental data is demonstrated by the small differences between the EoS coefficients obtained by the refinement and by the F_E-f_E plot of Figure 2 (K_{T0} = 122.9(6) GPa, K' = 4.9(2); the intercept corresponds to the bulk modulus whereas the slope of the straight line provides the first pressure derivative as in Angel (2001).

A parameterized form of the BM3 EoS was used to determine the axial moduli of *a*, *b*, and *c* again using EoS-FIT5.2. Equation-of-state coefficients together with the relative axial compressibilities are reported in Table 7. The anisotropy scheme, using the data reported in Table 7, is $K_c \leq K_a \leq K_b$, with an anisotropy ratio 1.04:1.00:1.07.

182

183 ***Crystal-structure evolution with pressure***

184 Figure 3 and Figure 4 show the evolution of the polyhedral volumes for M1, M11, M2 and M21
185 sites as a function of pressure. Relatively to the M2 and M21 polyhedra we observe a continuous
186 decrease of volume with pressure by about 6.4 and 6.9%, respectively (Fig. 4). The M2 polyhedron
187 shows a large deformation: the M2-O31 bond length shows a strong decrease close to 4.5% (see
188 Table 6); for the M21 polyhedron the M21-O32 bond length decreases even more with a reduction
189 by about 5.7% (see Table 6). This strong difference could explain the slightly greater volumetric
190 reduction of the M21 polyhedron.

191 The M1 and M11 polyhedra show lower volume decrease (by about 5.7 and 6.1%, respectively)
192 than M2 sites. The M11 polyhedron is slightly softer than M1 and this should be due to the greater
193 compressibility of the two bond lengths M1-O11 and M1-O22, which show a decrease by 2 and
194 3.3%, respectively, against the M11-O21 and M11-O12, which decrease by 1.2 and 3%,
195 respectively (see Table 6). In Figure 3 and Figure 4 it is possible to note that both M1 and M2
196 polyhedra show a slight but significant change in slope at about 4 GPa. Such a behavior cannot be
197 explained in terms of bond lengths compression anomaly but much likely to the tilt angle [defined
198 as the out-of-plane tilting of the basal face of the tetrahedral with respect to the plane (100) (see
199 Cameron et al. 1973)] variation as a function of pressure. In fact, in Figure 5 both the tilt angles of
200 TA and TB show a slope change between 2 and 4 GPa.

201 Concerning the TA and TB tetrahedra, they show a small decrease up to the maximum pressure
202 reached during the experiments, as expected for such usually very rigid polyhedra as a function of
203 pressure. However, a slight difference in compressibility between TA and TB is found (2.2 and
204 0.9%, respectively, up to 7.3 GPa).

205 The O3-O3-O3 angle, defining the tetrahedral chain kinking, linearly decreases by about 1.7% up to
206 6 GPa and then it seems to remain constant up to the maximum pressure reached.

207

DISCUSSION

The value of K_{T0} of our sample, obtained using a BM3-EoS, was plotted versus composition expressed in molar percentage of jadeite in Figure 6. In this Figure, pure value for jadeite is from Nestola et al. (2006), which is very close to McCarty et al. (2008) value. We decided to use Nestola et al. (2006) data because their data have been obtained using the same experimental techniques as those used in this work and thus the data are reliably comparable. Diopside is from Gavrilenko et al. (2010). Their data are the most recent on diopside compressibility and were calculated with the same experimental techniques used in this work (and using a BM3-EoS). These authors investigated two diopside samples: a first sample, Di_0 with K_{T0} (GPa) = 106(1) shows a not pure diopside composition (e.g. a limited excess of Mg) while a second sample, Di_{600} with K_{T0} (GPa) = 108(1) is hydrated (e.g. 600 ppm). However, it appears clear that both samples, in spite of their non purity, do not show any significant bulk modulus deviation from synthetic diopside by Tribaudino et al. (2000), K_{T0} (GPa) = 105.1(9), from the of value of K_{T0} (GPa) = 108 GPa computed from the adiabatic bulk modulus reported by Levien et al. (1979), and from the value extrapolated by Boffa Ballaran et al. (2009) on a pure diopside, K_{T0} (GPa) = 107.4(1). In Figure 6, the data referring to $Jd_{100}Di_0$, $Jd_{50}Di_{50}$ and Jd_0Di_{100} lie on a well defined bulk modulus vs. composition trend, which shows a clear curvature at intermediate composition. Along the jadeite-diopside solid solution the bulk modulus K_{T0} decreases by about 9% from 134.0(7) GPa for jadeite to the value of 122(1) GPa for our sample down to 106(1) GPa for diopside with a total decrease of about 21%. The value of bulk modulus from Pavese et al. (2001), lies very close to the trend in Figure 6. In the same figure the data from Nishihara et al. (2003), K_{T0} (GPa) = 126(1), and from sample SBB-1, K_{T0} (GPa) = 129(3), and SDC-1 K_{T0} (GPa) = 139(4) by McCormick et al. (1989) are also reported. They are not strictly relative to a $Jd_{50}Di_{50}$ composition and were calculated using a BM2-EoS with K' assumed to be 4. The recalculation of their data, using a BM3-EoS for purpose of comparison with our data led to a negative value of K'. Moreover, sample SBB-1 by McCormick et al. (1989) and sample by

Nishihara et al. (2003) contain 13 and 9% of Ca-Eskola ($Ca_{0.5}\square_{0.5}AlSi_2O_6$, vacancy-rich end-member) respectively. Regarding samples by McCormick et al. (1989), as already observed by the authors "there is a significant difference in the compression of the two omphacites, with the vacancy-rich pyroxene (SBB-1) being more compressible than the vacancy-poor pyroxene (SDC-1)". At any rate, the effect on the compressibility of the presence of Ca-Ts ($CaAl_2Si_2O_6$ end member) cannot be neglected. In fact the samples that more deviate from the trend are those containing the greater percentage of Ca-Ts: 6.2% and 4.6% for SDC-1 and Nishihara et al. (2003) samples, respectively. The influence of tetrahedral Al on the bulk-modulus was already evidenced by Nestola et al. (2008b) for an aluminum-rich ortopyroxene, where significant stiffening was reported.

Concerning the first pressure derivative, K', it increases nearly linearly as a function of the diopside content from 4.4(1) of jadeite, Nestola et al. (2006) to 5.1(3) (our study) to pure diopside 6.1(5) (Gavrilenko et al. 2010) as found for jadeite – hedenbergite join (Nestola et al. 2008a). It is well known (see Angel 2001) that the bulk modulus and its first pressure derivative strongly correlate to more than 95%; such correlation often covers the real errors in determining both the parameters as during the least squares refinement they are considered as two independent parameters. In this light, in order to better understand the K_{T0} - K' correlation along the Jd-Di join a series of confidence ellipses in the parameter space was constructed following Angel (2001) and shown in Figure 7. The confidence ellipse was calculated for our sample, as well as for diopside (Gavrilenko et al. 2010), omphacite (Pavese et al. 2001) and jadeite (Nestola et al. 2006) for a 68.3% confidence level. In this figure it is possible to note that for all the four samples a negative correlation is present and that, considering the extension of the ellipses, the errors on the K_{T0} and K' must be reconsidered for all samples: for jadeite (Nestola et al. 2006) the errors in K_{T0} and K' increase only slightly from 0.7 GPa and 0.1 to 1 GPa and 0.3, respectively; for diopside (Gavrilenko et al. 2010) the errors in K_{T0} and K' increase from 1 GPa and 0.5 to 2 GPa and 0.7, respectively; for our omphacite samples the errors in K_{T0} and K' increase from 1 GPa and 0.3 to 2 GPa and 0.5, respectively; finally for the

omphacite sample by Pavese et al. (2001) the errors increase from 2.5 GPa and 0.6 to 4 GPa and 1.0, respectively, suggesting that some non hydrostaticity could be the cause of such strong increase in the K_{T0} and K' errors due to their correlation. In fact Pavese et al. (2001) obtained their EoS by X-ray powder diffraction up to 13 GPa using synchrotron radiation and nitrogen as a pressure medium. As demonstrated by Angel et al. (2007) nitrogen is a non hydrostatic pressure medium for pressures above 2-3 GPa.

In order to explain the difference in compressibility along the jadeite – diopside solid solution the structural deformation mechanisms along the join has to be taken into account. As mentioned by Thompson and Downs (2008) and Nestola et al. (2008a) the main three deformation mechanisms can be described as following: isotropic scaling of the structure, tetrahedral chain kinking and narrowing of the M1 chain along the **b** direction. For our omphacite sample, we observed the following high-pressure behavior: i) concerning the isotropic scaling of the structure, as reported in Table 7, the axial bulk modulus anisotropy is relatively limited with differences lower than 7%; ii) the tetrahedral chain shows a significant contraction of about 0.47°/GPa, thus affecting the M2-O31 bond length, which shows the strongest contraction compared with the other bond lengths (by about 0.017 Å/GPa); iii) the angle between O21-O22-O21, which can be used as an indication of the narrowing of the M1 chain (see Figure 8) increases by 1.3° up to 7.34 GPa. (Table 6).

In order to verify if we could find any systematic structural deformation mechanism along the diopside-jadeite join we compared our sample with the two end-members diopside and jadeite (Thompson and Downs 2008 and Nestola et al. 2008a). In particular, relatively to the contraction of the tetrahedral chain and the M1 chain narrowing, we did not find a significant different behavior of our sample compared to that of the end-members. Taking into account the linear compressibility [expressed as $\beta = ((V-V_0)/V_0)/\Delta P$] of the structural M1 and M2 polyhedra, a possible comparison of our *P*2/*n* omphacite with the two end members can be performed on the basis of the site population of the structural sites. Regarding the M1 polyhedra, in an ordered *P*2/*n* omphacite, the M11 of omphacite is similar to the M1 of jadeite due to its aluminum content ($X^{Al}_{M11} = 0.957$) while M1 for

its Mg content (X^{Mg}_{M1} = 0.837) is similar to M1 of diopside. Concerning M2 polyhedra, the comparison of M2 in omphacite to M2 of jadeite and M21 polyhedron to M2 of diopside is more questionable due to the partial order of Na and Ca in the structural sites of the ordered omphacite. The linear compressibility of M2 of omphacite shows the same value than that of jadeite (β_{M2} = 0.0088 GPa^{-1} and β_{M2} = 0.0090 GPa^{-1}, respectively) whereas its M11 linear compressibility is greater (β_{M11} of omphacite = 0.0083 GPa^{-1}, β_{M1} of jadeite = 0.0065 GPa^{-1}). This supports the evidence of a lower bulk modulus for the *P*2/*n* omphacite (K_{T0} omphacite is 122 GPa with respect to the K_{T0} of 134 for jadeite). However, similar relationships has not been found comparing omphacite and diopside. In fact, whereas the M1 linear compressibility is identical for both samples (β_{M1} = 0.0077 GPa^{-1}), the value of M21 of omphacite is significantly greater than that of M2 of diopside (β_{M21} = 0.0094 GPa^{-1} and β_{M2} = 0.0080 GPa^{-1} respectively). This is in contrast with the evidence of a greater bulk modulus for the *P*2/*n* omphacite with respect to diopside (K_{T0} = 106).

If the variation of the M1 and M2 polyhedral volumes with pressure, as reported in Figure 3 and Figure 4, is considered, a linear fitting can be used. With this approach, regarding the M1 polyhedra, the coefficient that describes the slope of the straight line confirms the similar behavior of M11 of omphacite with M1 of jadeite [0.079(9) vs. 0.061(8), respectively] and of M1 of omphacite and diopside [0.093(7) vs. 0.091(2), respectively]. Concerning the M2 polyhedra, the same coefficient does confirm the similarity between the M2 of omphacite and jadeite [0.22(2) vs. 0.22(3), respectively] but shows the same contrast between M21 of omphacite and M2 of diopside [0.25(2) vs. 0.205(7), respectively] already observed above. It seems apparent that while about 25% of Ca in M2 of omphacite does not affect the compressibility of this polyhedron with respect to that of jadeite, the same amount of Na in M21 of omphacite makes the compressibility of the polyhedron to increase with respect to that of M2 of diopside. It is remarkable that the averaged effect of the various polyhedra is, by all means, intermediate between those of Jd and Di (reported also in Figs. 3 and 4) as it is for the bulk modulus.

ACKNOLEDGEMENTS

This work was also funded by the Italian Ministry of University and Research (MIUR), grant no. ????????. [FAR] Roberto Gastoni CNR-Pavia is thanked for sample preparation for EMPA analyses and R. Carampin of CNR-Padova for WDS electron microprobe facilities.

REFERENCES

Agee, C.B. (1999) Phase transformations and seismic structure in the upper mantle and transition zone. In R.J. Hemley, Ed., Ultrahigh-pressure mineralogy: physics and chemistry of the earth's deep interior, Reviews in Mineralogy and Geochemistry, Mineralogical Society of America and Geochemical Society, 37, 165-203.

Angel, R.J., Allan, D.R., Miletich, R., and Finger, L.W. (1997) The use of quartz as an internal pressure standard in high pressure crystallography. Journal of Applied Crystallography, 30, 461–466.

Angel, R.J. (2001) Equations of State. In R.M. Hazen and R.T. Downs, Eds., High-Temperature and High-Pressure Crystal Chemistry, Reviews in Mineralogy and Geochemistry, Mineralogical Society of America, 41, 35–39.

——— (2002) EOSFIT V5.2 program. Crystallography Laboratory. Virginia Tech, U.S.A.

——— (2004) Absorption corrections for diamond-anvil cells implemented in the software package Absorb 6.0. Journal of Applied Crystallography, 37, 486–492

Angel R.J., and Finger, L.W. (2011) SINGLE: a program to control single-crystal diffractometers. Journal of applied Crystallography, 44, 247-251.

Angel, R.J., Bujak, M., Zhao, J., Gatta, D., Jacobsen, S.D. (2007) Effective hydrostatic limits of pressure media for high-pressure crystallographic studies. Journal of Applied Crystallograpy, 40, 26–32

Balić-Žunić, T. and Vicković, I. (1996) IVTON-program for the calculation of geometrical aspects of crystal structures and some crystal chemical applications. Journal of Applied Crystallography, 29, 305–306.

Bindi. L., Downs, R.T., Harlow, G.E., Safonov, O.G., Litvin, Y.A., Perchuk, L.L., Uchida, H., Menchetti, S. (2006) Compressibility of synthetic potassium-rich clinopyroxene: In-situ high-pressure single-crystal X-ray study. American Mineralogist, 91, 802-808.

Birch, F. (1947) Finite elastic strain of cubic crystals. Physical Review, 71, 809–824.

Blessing R.H. (1995): An empirical correction for absorption anisotropy. Acta Crystallographica, 51, 33-38.

Boffa Ballaran, T., Carpenter, M.A., Domeneghetti, M.C. and Tazzoli, V., (1998) Structural mechanisms of solid solution and cation ordering in augite-jadeite pyroxenes: I. A macroscopic perspective. American Mineralogist, 83, 419–433.

Boffa Ballaran, T., Nestola, F., Tribaudino, M., and Ohashi, H. (2009) Bulk modulus variation along the diopside–kosmochlor solid solution. European Journal Mineralogy, 21, 591–597.

Cameron, M., Sueno, S., Prewitt, C.T., and Papike, J.J. (1973) High temperature crystal chemistry of acmite, diopside, hedenbergite, jadeite, spodumene, and ureyite. American Mineralogist, 58, 594–618.

Carpenter, M.A., Domeneghetti, M.C., and Tazzoli, T. (1990) Application of Landau theory to cation ordering in omphacite I: Equilibrium behavior. European Journal of Mineralogy, 2, 7-18.

Downs, R.T. (2003) Topology of the pyroxenes as a function of temperature, pressure, and composition as determined from the procrystal electron density. American Mineralogist, 88, 556–566.

Gavrilenko, P., Boffa Ballaran, T. and Kepler, H. (2010) The effect of Al and water on the compressibility of diopside. American Mineralogist, 95, 608–616.

Hawthorne, F.C., Ungaretti, L., and Oberti, R. (1995) Site populations in minerals: terminology and presentation of results of crystal-structure reÞ nement. Canadian Mineralogist, 33, 907-911.

King, H.E. and Finger, L.W. (1979) Diffracted beam crystal centering and its application to high-pressure crystallography. Journal of Applied Crystallography, 12, 374–378.

Koch-Muller, M., Matsyuk, S.S., Wirth, R. (2004) Hydroxyl in omphacites and omphacitic clinopyroxenes of upper mantle to lower crustal origin beneath the Siberian platform. American Mineralogist, 89, 921-931

Levien, L., Weidner, D.J., Prewitt, C.T. (1979): Elasticity of diopside. Phys. Chem. Minerals, 4, 105–113.

McCarty, A.C., Downs, R.T. and Thompson R.M. (2008) Compressibility trends of the clinopyroxenes, and in-situ high-pressure single-crystal X-ray diffraction study of jadeite. American Mineralogist, 93, 198-209

McCormick, T.C., Hazen, R.M., Angel, R.J. (1989) Compressibility of omphacite to 60 kbar: Role of vacancies. American Mineralogist, 74, 1287-1292.

Miletich, R., Allan, D.R., and Kuhs, W.F. (2000) High-pressure single-crystal techniques. In R.M. Hazen and R.T. Downs, Eds., High-Temperature and High-Pressure Crystal Chemistry, Reviews in Mineralogy and Geochemistry, Mineralogical Society of America, 41, 445–519. .

Nestola, F., Ballaran, T.B., Tribaudino, M., Ohashi, H. (2005) Compressional behaviour of $CaNiSi_2O_6$ clinopyroxene: bulk modulus systematic and cation type in clinopyroxenes. Physics and Chemistry of Minerals, 32, 222-227.

Nestola, F., Boffa Ballaran, T., Liebske, C., Bruno, M., Tribaudino, M. (2006) High-pressure behaviour along the jadeite $NaAlSi_2O_6$–aegirine $NaFeSi_2O_6$ solid solution up to 10 GPa. Physics and Chemistry of Minerals, 33, 417–425.

Nestola, F., Tribaudino, M., Boffa Ballaran, T., Liebske, C. and Bruno, M. (2007) The crystal structure of pyroxenes along the jadeite–hedenbergite and jadeite–aegirine joins. American Mineralogist, 92, 1492-1501.

Nestola, F., Boffa Ballaran, T., Liebske, C., Thompson, R. and Downs R.T. (2008a) The effect of the hedenbergitic substitution on the compressibility of jadeite. American Mineralogist, 93 1005–1013.

Nestola, F., Ballaran, T.B., Balic-Zunic, T. (2008b) The high-pressure behavior of an Al- and Fe-rich natural orthopyroxene. American Mineralogist, 93, 644-652.

Nestola, F., Smyth, J.R., Parisatto, M., Secco, L., Princivalle, F., Bruno, M., Prencipe, M. Dal Negro, A. (2009) Effects of non-stoichiometry on the spinel structure at high pressure: Implications for Earth's mantle mineralogy. Geochimica and Cosmochimica Acta, 73, 489-492.

Nestola. F., Boffa Ballaran, T., Angel, R.J., Zhao, J., Ohashi, H. (2010) High-pressure behaviour of Ca/Na clinopyroxenes: The effect of divalent and trivalent 3d-transition elements. American Mineralogist, 95, 832-838.

Nishihara, Y., Takahashi, E., Matsukage, K. and Kikegawa, T. (2003) Thermal equation of state of omphacite. American Mineralogist, 88, 80–86.

Origlieri, M.J, Downs, R.T., Thompson, R.M., Pommier, C.J.S., Denton, M.B. and Harlow, G.E. (2003) High-pressure crystal structure of kosmochlor $NaCrSi_2O_6$ and systematics of anisotropic compression in pyroxenes. American Mineralogist, 88, 1025–1032 and 1632.

Pavese, A., Bocchio, R., Ivaldi, G. (2000) In situ high temperature single crystal X-ray diffraction study of a natural omphacite. Mineralogical Magazine, 64, 983–993.

Pavese, A., Diella, V., Devy D., Hanfland, M. (2001) Synchrotron X-ray diffraction study of a natural *P*2/*n* omphacites at high pressure conditions. Physics and Chemistry of Minerals, 28, 9-16.

Pouchou J.L. and Pichoir F. (1991) Quantitative analysis of homogeneous or stratified microvolumes applying the model "PAP." In Electron probe quantitation, edited by Heinrich K. F. J. and Newbury D. E. New York: Plenum Press. pp. 31–75.

Ralph, R.L. and Finger, L.W. (1982) A computer program for refinement of crystal orientation matrix and lattice constraints from diffractometer data with lattice symmetry constraints. Journal of Applied Crystallography, 15, 537–539.

Sheldrick, G.M. (1996) SADABS. University of Go¨ttingen: Go¨ttingen, Germany.

Sheldrick, G.M. (2008) A short history of SHELX. Acta Crystallographica, A64, 112-122

Thompson, R.M. and Downs, R.B. (2008) The crystal structure of diopside at pressure to 10 GPa. American Mineralogist, 93, 177–186.

Thompson, R.M., Downs, R.T. and Redhammer, G.J. (2005) Model pyroxenes III: Volume of *C*2/*c* pyroxenes at mantle P, T, and x. American Mineralogist, 90, 1840.1851.

Wilson, A.J.C. (1995) International Tables for Crystallography. Volume C. Kluwer Academic Publishers, Dordrecht.

Zema, M., Domeneghetti, M.C., Molin, G.M. et al. (1997) Cooling rates of diogenites: A study of Fe^{2+}-Mg ordering in orthopyroxene by single-crystal x-ray diffraction. Meteoritics and Planetary Science, 32, 855-862

Table and Figure captions

Table 1. Electron microprobe analysis and formula in atoms per formula unit (apfu) based on six oxygen atoms for omphacite crystal N.4 (average of 15 spots)

Table 2. Unit-cell parameters at different pressure values for crystal N.4

Table 3. Structure refinement details (the relative unit-cell parameters are reported in Table 2) for crystal N.4

Table 4. Site populations and degree of order of crystal N4 in air.

Table 5. Fractional coordinates and displacement parameters for the crystal N4

Table 6. Selected bond lengths (Å) and angles (°) in *P*2/n structure for the sample studied in this work.

Table 7. Equation of state coefficients for N4 usign a third order Birch-Murnagnan equation.

Figure 1. Evolution of the **a)** unit-cell parameters and **b)** unit-cell volume as a function of pressure for all the samples investigated. The symbols used are larger than the errors. The curve plotted in **b)** is the real Equation of State for the sample.

Figure 2. $F_E - f_E$ plot {$F_E = P/3 \times f_E \times (1 + 2f_E)5/2$ and $f_E = [(V_0/V)2/3 - 1]/2$, see Angel 2000} for the sample studied in this work.

Figure 3. Evolution of M1 polyhedral volumes as a function of pressure.

Figure 4. Evolution of M2 polyhedral volumes as a function of pressure.

Figure 5. Evolution of the tilt angle as a function of pressure for the two tetrahedral chains TA and TB**.**

Figure 6. Evolution of K_{T0} as a function of composition along the diopside-jadeite join.

Figure 7. Confidence ellipse for the equation of state of the sample studied in this work and for other samples studied along the diopside-jadeite join.

Figure 8. Part of the crystal-structure of the sample studied in this work viewed along the [100] direction. The octahedral M1 and M11 sites are showed. The black line corresponds to the O21-O22-O21 angle.

Equations

Eqn. 1 $$Q_{M1}^{occ} = \frac{\left|\frac{(Al+Fe^{3+})_{M1}-(Al+Fe^{3+})_{M11}}{\sum(Al+Fe^{3+})}\right| + \left|\frac{(Mg+Fe^{2+})_{M1}-(Mg+Fe^{2+})_{M11}}{\sum(Mg+Fe^{2+})}\right|}{2}$$

Eqn. 2 $$Q_{M2}^{occ} = \frac{\left|\frac{Na_{M2}-Na_{M21}}{\sum Na}\right| + \left|\frac{Ca_{M2}-Ca_{M21}}{\sum Ca}\right|}{2}$$

Eqn. 3 $$Q_{M1}^{dist} = \left|\frac{\langle M1-O\rangle-\langle M11-O\rangle}{\frac{1}{2}(\langle M1-O\rangle+\langle M11-O\rangle)}\right|$$

Eqn. 4 $$Q_{M2}^{dist} = \left|\frac{\langle M2-O\rangle-\langle M21-O\rangle}{\frac{1}{2}(\langle M2-O\rangle+\langle M21-O\rangle)}\right|$$

Table 1. Electron microprobe analysis and formula in atoms per formula unit (apfu) based on six oxygen atoms for omphacite crystal N.4 (average of 15 spots)

% oxides		*a.p.f.u.*	
SiO_2	56.1(4)	Si	1.968(7)
TiO_2	0.11(2)	Al^{IV}	0.032(7)
Al_2O_3	13.1(2)	Al^{VI}	0.510(9)
Cr_2O_3	0.03(3)	Fe^{3+}	0.002(3)
FeO	2.33(6)	Fe^{2+}	0.067(4)
MnO	0.03(2)	Mg	0.448(8)
MgO	8.6(1)	Mn	0.0009(6)
CaO	13.0(2)	Ti	0.0030(6)
Na_2O	6.9(2)	Cr	0.0009(9)
K_2O	0.004(5)	Ca	0.490(7)
total	100.3(5)	Na	0.47(1)
		K	0.0002(2)
		total	3.99(1)

Table 2. Unit-cell parameters at different pressure values for crystal N.4

P (GPa)	*a* (Å)	*b* (Å)	*c* (Å)	*β* (Å)	*V* (Å^3)
in air	9.5613(4)	8.7578(4)	5.2543(2)	106.953(1)	420.85(3)
0.00010(1)	9.568(1)	8.7608(15)	5.2561(8)	106.995(10)	421.36(9)
0.449(6)	9.5541(5)	8.7481(7)	5.2482(3)	106.895(4)	419.71(4)
1.245(8)	9.5346(5)	8.7292(7)	5.2376(4)	106.809(5)	417.30(4)
1.78(1)	9.5198(4)	8.715(1)	5.2296(6)	106.744(8)	415.48(7)
2.74(1)	9.4973(4)	8.6914(6)	5.2163(3)	106.630(4)	412.57(4)
3.41(1)	9.4810(5)	8.6745(6)	5.2078(3)	106.567(4)	410.52(4)
4.14(1)	9.4645(4)	8.6576(6)	5.1981(3)	106.497(4)	408.40(3)
5.02(1)	9.4452(6)	8.6368(9)	5.187(4)	106.412(6)	405.89(5)
5.89(1)	9.4278(6)	8.6165(7)	5.1769(4)	106.334(5)	403.57(4)
6.456(9)	9.4156(6)	8.6044(8)	5.1695(4)	106.228(5)	402.00(4)
7.11(2)	9.403(5)	8.5913(7)	5.162(3)	106.234(4)	400.37(4)
7.34(2)	9.3992(6)	8.5857(7)	5.1593(3)	106.216(5)	399.79(4)
7.55(2)	9.3949(6)	8.5832(9)	5.1574(5)	106.210(6)	399.35(5)

Table 3. Structure refinement details (the relative unit-cell parameters are reported in Table 2) for crystal N.4

P (GPa)	*in air*	0	1.78	4.14	5.89	7.34
2θ max (°)	78	60	60	60	60	60
*R*1 (%)	2.38	8.4	8.31	9.14	8.25	10.38
n. of I/σ >4	2068	315	307	306	301	285
n. relf. tot.	2164	534	519	512	514	497
ref. param.	110	45	45	45	45	45
GooF	1.151	1.193	1.159	1.222	1.196	1.223
WR^2 (%)	6.1	21.5	23.0	24.2	23.0	28.6

Table 4. site populations and degree of order of crystal N4 in air

T	Si	1.9639	**M2**	Ca	0.2531
	Al	0.0361		Na	0.7365
				Fe	0.0104
M1	Mg	0.8370			
	Fe	0.0921	**M21**	Ca	0.7128
	Al	0.0693		Na	0.2309
	Mn	0.0016		Mg	0.0563
M11	Mg	0.0157	Q^{occ}_{M1}		0.8956
	Fe	0.0199			
	Al	0.9572	Q^{occ}_{M2}		0.4993
	Ti	0.0058			
	Cr	0.0015	Q^{dist}_{M1}		0.0689
			Q^{dist}_{M2}		0.0161

Table 7. Equation of state coefficients for N4 using a third order Birch-Murnagnan equation.

$\mathbf{a_0}$	9.5685(5)	$\mathbf{b_0}$	8.7618(7)	$\mathbf{c_0}$	5.2558(3)	$\mathbf{V_0}$	421.43(4)
$\mathbf{Ka_0}$	112(2)	$\mathbf{Kb_0}$	107(2)	$\mathbf{Kc_0}$	115(2)	$\mathbf{K_{TO}}$	122(1)
K'	7.6(5)	**K'**	3.9(5)	**K'**	4.9(5)	**K'**	5.1(3)

Table 5. Fractional coordinates and displacement parameters for the crystal N4

P(GPa)		*in air*	0	1.77	4.14	5.89	7.34
M1	x	0.25	0.25	0.25	0.25	0.25	0.25
	y	0.15953(4)	0.1592(5)	0.1600(5)	0.1599(5)	0.1607(5)	0.1560(6)
	z	0.25	0.25	0.25	0.25	0.25	0.25
	Uiso	0.0069(1)	0.012(1)	0.012(1)	0.009(1)	0.009(1)	0.010(1)
M11	x	0.25	0.25	0.25	0.25	0.25	0.25
	y	0.34753(4)	0.3481(5)	0.3471(5)	0.3465(5)	0.3461(5)	0.3451(6)
	z	0.75	0.75	0.75	0.75	0.75	0.75
	Uiso	0.0058(1)	0.007(1)	0.008(1)	0.009(1)	0.009(1)	0.012(1)
M2	x	0.25	0.25	0.25	0.25	0.25	0.25
	y	0.55220(5)	0.5521(6)	0.5532(6)	0.5541(6)	0.5548(6)	0.5553(6)
	z	0.25	0.25	0.25	0.25	0.25	0.25
	Uiso	0.0103(1)	0.016(1)	0.014(1)	0.015(1)	0.014(1)	0.013(1)
M21	x	0.25	0.25	0.25	0.25	0.25	0.25
	y	0.95046(3)	0.9502(4)	0.9491(4)	0.9474(4)	0.9470(4)	0.9470(5)
	z	0.75	0.75	0.75	0.75	0.75	0.75
	Uiso	0.01079(9)	0.013(1)	0.013(1)	0.013(1)	0.012(1)	0.013(1)
Si1	x	0.53939(2)	0.5390(3)	0.5390(4)	0.5390(4)	0.5393(4)	0.5392(5)
	y	0.34783(2)	0.3485(3)	0.3493(3)	0.3484(4)	0.3490(3)	0.3495(4)
	z	0.22638(4)	0.2261(5)	0.2256(5)	0.2256(5)	0.2252(6)	0.2253(6)
	Uiso	0.00528(6)	0.0099(8)	0.0093(8)	0.0083(9)	0.0084(9)	0.010(1)
Si2	x	0.53731(2)	0.5368(3)	0.5378(4)	0.5376(4)	0.5375(4)	0.5378(5)
	y	0.16263(2)	0.1632(3)	0.1628(3)	0.1613(4)	0.1609(3)	0.1608(4)
	z	0.73036(4)	0.7307(5)	0.7308(5)	0.7303(5)	0.7291(6)	0.7293(6)
	Uiso	0.00510(6)	0.0086(8)	0.0085(8)	0.0084(9)	0.0095(9)	0.010(1)
O11	x	0.36286(6)	0.3626(8)	0.3631(8)	0.3627(9)	0.3616(9)	0.361(1)
	y	0.33887(7)	0.3358(8)	0.3374(8)	0.3390(8)	0.3398(7)	0.3392(8)
	z	0.1199(1)	0.118(1)	0.119(1)	0.122(1)	0.119(1)	0.120(1)
	Uiso	0.0075(1)	0.011(2)	0.011(2)	0.007(2)	0.007(2)	0.004(2)
O12	x	0.36109(6)	0.3623(7)	0.3618(8)	0.3606(9)	0.3610(9)	0.362(1)
	y	0.17821(7)	0.1769(8)	0.1762(8)	0.1758(8)	0.1749(9)	0.175(1)
	z	0.6483(1)	0.649(1)	0.650(1)	0.649(1)	0.650(1)	0.653(2)
	Uiso	0.0073(1)	0.010(2)	0.010(2)	0.011(2)	0.015(2)	0.016(2)
O21	x	0.61503(7)	0.6168(9)	0.6154(9)	0.6164(9)	0.6157(9)	0.617(1)
	y	0.51010(7)	0.5109(8)	0.5103(8)	0.5137(9)	0.5135(8)	0.517(1)
	z	0.3090(1)	0.310(1)	0.312(1)	0.312(1)	0.314(1)	0.315(1)
	Uiso	0.0086(1)	0.013(2)	0.013(2)	0.012(2)	0.012(2)	0.012(2)
O22	x	0.60598(7)	0.6050(8)	0.6051(9)	0.6054(9)	0.6061(9)	0.607(1)
	y	0.99774(7)	0.9984(8)	0.9975(8)	0.9944(8)	0.9941(8)	0.9926(9)
	z	0.8048(1)	0.804(1)	0.806(1)	0.809(1)	0.811(1)	0.813(1)
	Uiso	0.0097(1)	0.011(2)	0.011(2)	0.009(2)	0.010(2)	0.012(2)
O31	x	0.60675(6)	0.6069(8)	0.6079(8)	0.6072(8)	0.6071(9)	0.607(1)
	y	0.26646(7)	0.2662(8)	0.2683(8)	0.2693(8)	0.2712(8)	0.2719(9)
	z	0.0041(1)	0.004(1)	0.002(1)	0.000(1)	_0.002(1)	_0.003(1)
	Uiso	0.0075(1)	0.009(2)	0.010(2)	0.008(2)	0.010(2)	0.010(2)
O32	x	0.59781(6)	0.5970(8)	0.5995(8)	0.6004(9)	0.6010(9)	0.600(1)
	y	0.24041(7)	0.2387(8)	0.2379(8)	0.2356(8)	0.2345(8)	0.235(1)
	z	0.4972(1)	0.498(1)	0.495(1)	0.494(1)	0.492(1)	0.491(1)
	Uiso	0.0081(1)	0.011(2)	0.011(2)	0.009(2)	0.012(2)	0.013(2)

Table 6. Selected bond lengths (Å) and angles (°) in *P*2/n structure for the sample studied in this work.

P(GPa)	*in air*	0.00	1.78	4.14	5.89	7.34
T1-O11	1.6178(6)	1.620(8)	1.609(8)	1.603(9)	1.612(9)	1.614(10)
T1-O21	1.5962(6)	1.606(8)	1.585(8)	1.612(8)	1.598(7)	1.618(9)
T1-O31	1.6510(6)	1.657(8)	1.654(8)	1.640(9)	1.630(9)	1.624(10)
T1-O32	1.6608(6)	1.675(6)	1.673(6)	1.666(7)	1.665(7)	1.652(8)
<T1 - O>	1.631(30)	1.640(32)	1.630(40)	1.630(28)	1.626(29)	1.627(17)
Volume ($Å^3$)	2.210(2)	2.24(2)	2.20(2)	2.20(2)	2.19(2)	2.19(3)
TQE	1.0059	1.0077	1.0077	1.0064	1.0065	1.0066
TAV (°)	25.6262	34.1313	33.8249	28.2997	28.1005	27.9951
TILT (°)	3.50(2)	3.9(2)	3.2(2)	3.2(2)	3.0(2)	2.3(3)
T2-O12	1.6185(6)	1.603(8)	1.610(8)	1.612(9)	1.603(10)	1.593(11)
T2-O22	1.5873(7)	1.585(8)	1.580(8)	1.588(8)	1.584(7)	1.594(9)
T2-O31	1.6670(6)	1.663(6)	1.660(6)	1.658(7)	1.663(7)	1.652(8)
T2-O32	1.6471(6)	1.637(7)	1.644(8)	1.641(8)	1.635(8)	1.632(10)
<T2 - O>	1.630(35)	1.622(35)	1.624(36)	1.625(31)	1.621(35)	1.618(29)
Volume ($Å^3$)	2.207(2)	2.18(2)	2.18(2)	2.19(2)	2.17(2)	2.16(3)
TQE	1.0051	1.0044	1.0041	1.0043	1.0046	1.0047
TAV (°)	21.556	18.5843	17.0801	18.0703	19.3477	19.9658
TILT (°)	1.92(2)	2.0(2)	1.6(2)	1.4(2)	1.3(2)	1.4(3)
M1-O11	2.1281(7)	2.144(8)	2.109(8)	2.094(9)	2.084(8)	2.073(9)
M1-O12	2.0587(6)	2.065(5)	2.061(5)	2.044(6)	2.045(7)	2.055(8)
M1-O22	2.0267(7)	2.036(9)	2.026(9)	1.998(9)	1.991(9)	1.968(10)
<M1- O>	2.071(46)	2.072(35)	2.065(37)	2.045(43)	2.040(42)	2.032(50)
Volume ($Å^3$)	11.603(7)	11.62(7)	11.51(7)	11.19(7)	11.10(8)	10.96(8)
TQE	1.0144	1.0139	1.0135	1.0134	1.0137	1.0143
TAV (°)	46.7793	46.1522	44.5324	43.4855	44.4995	45.5613
M11-O11	1.9299(6)	1.924(5)	1.920(5)	1.927(6)	1.906(6)	1.903(7)
M11-O12	1.9859(6)	2.004(8)	1.986(8)	1.967(8)	1.960(9)	1.944(10)
M11-O21	1.8840(6)	1.866(9)	1.878(9)	1.844(9)	1.848(9)	1.825(10)
<M11 - O>	1.933(46)	1.931(62)	1.928(49)	1.913(56)	1.905(50)	1.891(54)
Volume ($Å^3$)	9.546(6)	9.51(6)	9.48(6)	9.24(7)	9.13(7)	8.93(7)
TQE	1.0066	1.0073	1.0065	1.0072	1.0067	1.0066
TAV (°)	21.3266	22.1401	20.631	22.0344	21.2417	20.2871
M2-O11	2.3564(7)	2.381(8)	2.365(8)	2.334(9)	2.323(8)	2.316(9)
M2-O21	2.3640(6)	2.358(6)	2.347(6)	2.343(6)	2.331(6)	2.326(7)
M2-O31	2.6919(7)	2.695(8)	2.649(8)	2.617(9)	2.586(9)	2.57(10)
M2-O32	2.4603(7)	2.475(8)	2.458(8)	2.454(8)	2.448(8)	2.441(9)
<M2- O>	2.47(14)	2.48(14)	2.45(13)	2.45(12)	2.42(11)	2.41(11)
Volume ($Å^3$)	24.63(1)	24.8(1)	24.2(1)	23.8(1)	23.4(1)	23.2(2)
M21-O12	2.3924(7)	2.390(8)	2.376(8)	2.366(8)	2.350(9)	2.34(10)
M21-O22	2.3866(7)	2.391(6)	2.380(6)	2.366(6)	2.351(6)	2.336(7)
M21-O31	2.4743(7)	2.471(7)	2.468(7)	2.457(7)	2.462(7)	2.468(9)
M21-O32	2.77506	2.773(8)	2.723(7)	2.672(8)	2.643(8)	2.64(10)
<M21- O>	2.51(17)	2.51(17)	2.49(15)	2.46(13)	2.45(13)	2.45(13)
Volume ($Å^3$)	25.92(1)	26.0(1)	25.4(1)	24.7(1)	24.4(1)	24.2(2)
O31-O32-O31	169.46(04)	168.7(4)	167.9(4)	166.9(4)	165.9(4)	166.0(5)
O21-O22-O21	63.19(01)	63.19(13)	63.24(14)	63.95(14)	64.01(13)	64.52(15)

bond lenght and volume data from IVTON program

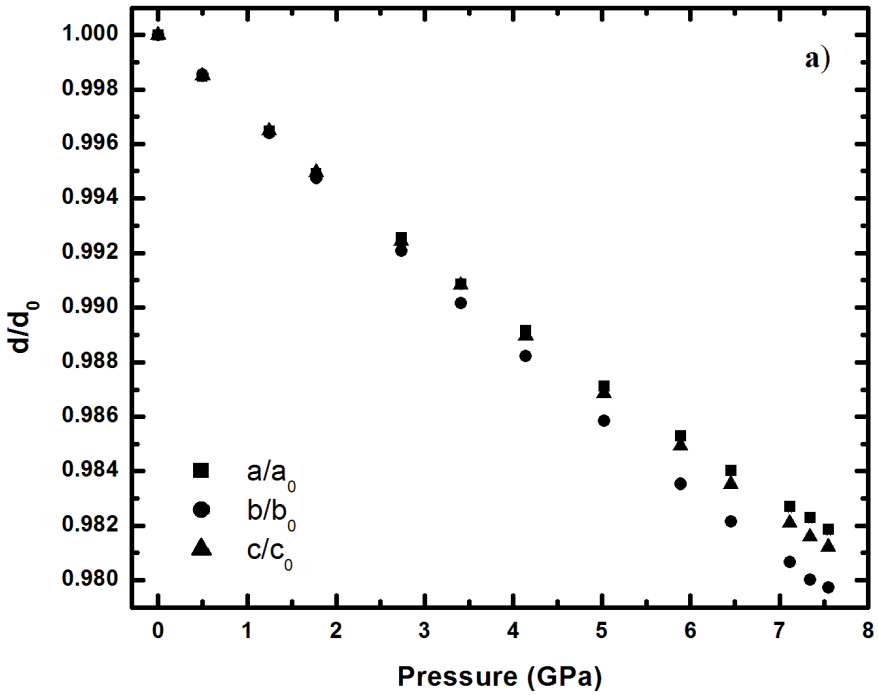

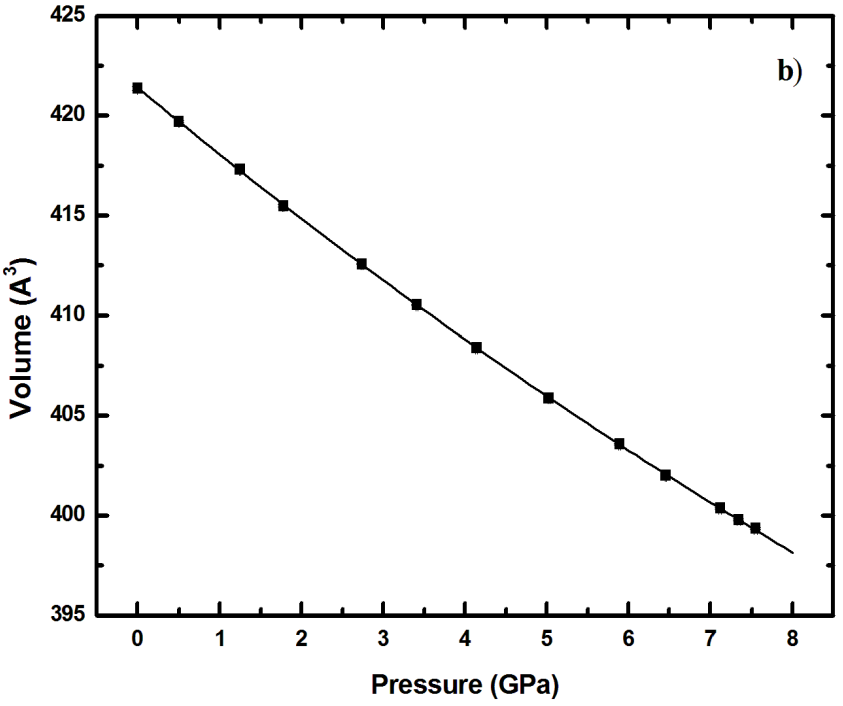

Figure 1. Evolution of the **a)** unit-cell parameters and **b)** unit-cell volume as a function of pressure for all the samples investigated. The symbols used are larger than the errors. The curve plotted in **b)** is the real Equation of State for the sample.

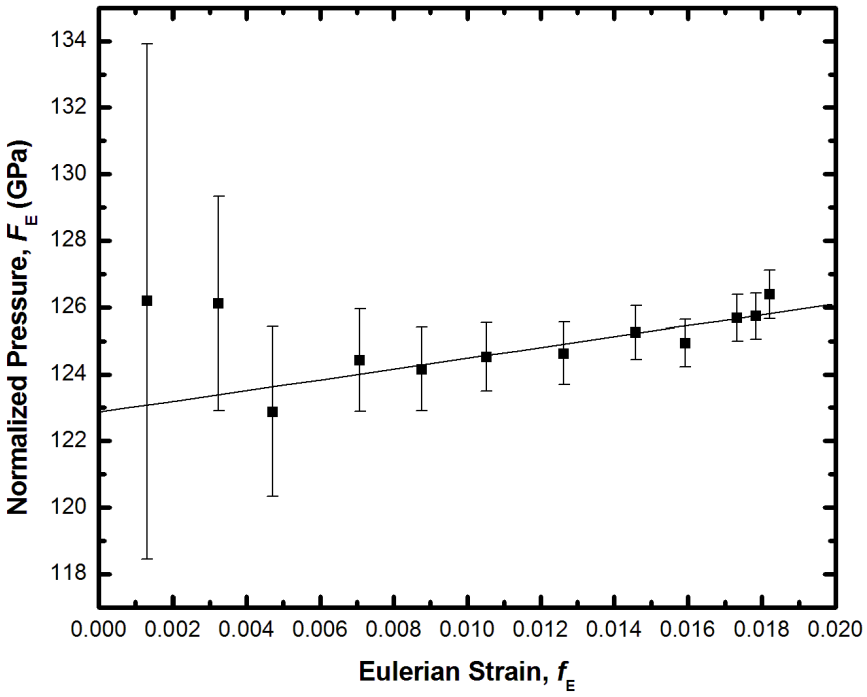

Figure 2. $F_E - f_E$ plot {$F_E = P/3 \times f_E \times (1 + 2f_E)5/2$ and $f_E = [(V_0/V)2/3 - 1]/2$, see Angel 2000} for the sample studied in this work

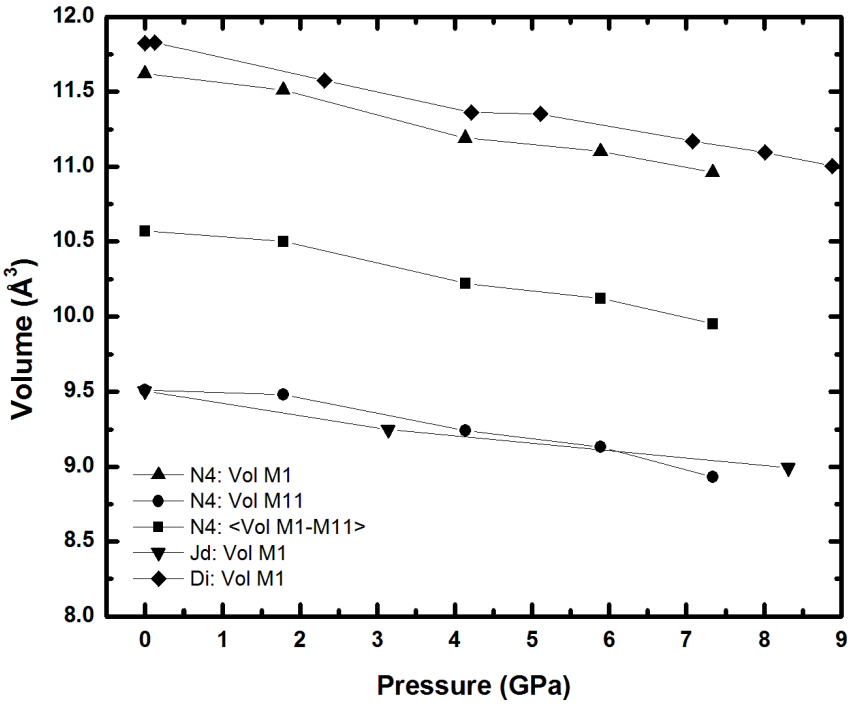

Figure 3. Evolution of M1 polyhedral volumes as a function of pressure.

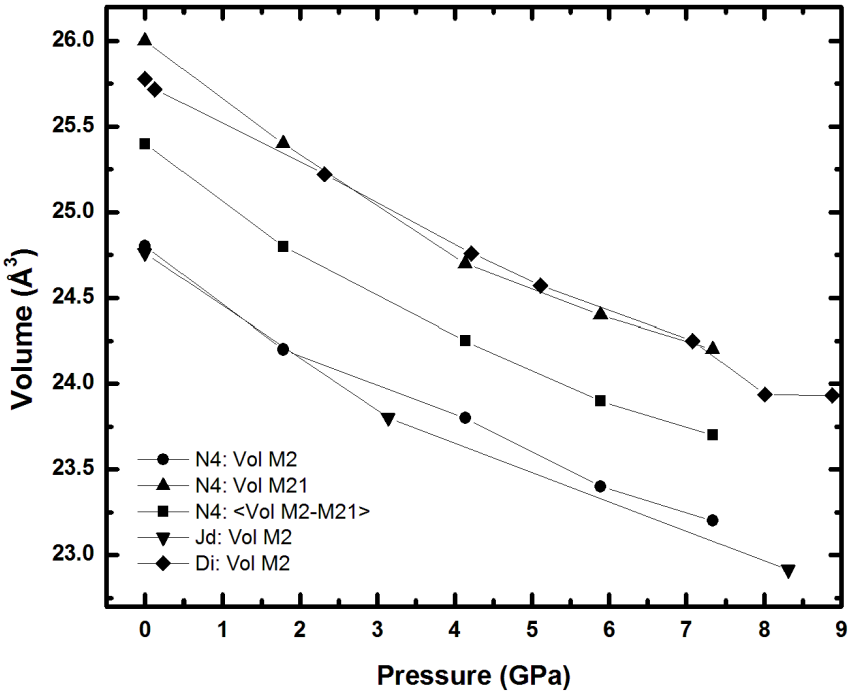

Figure 4. Evolution of M2 polyhedral volumes as a function of pressure.

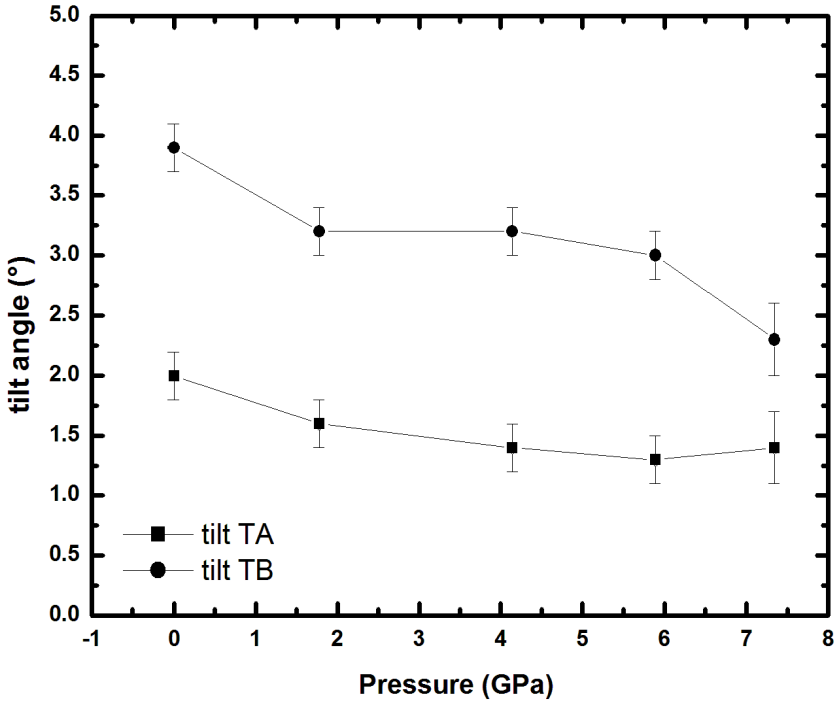

Figure 5. Evolution of the tilt angle as a function of pressure for the two tetrahedral chains TA and TB**.**

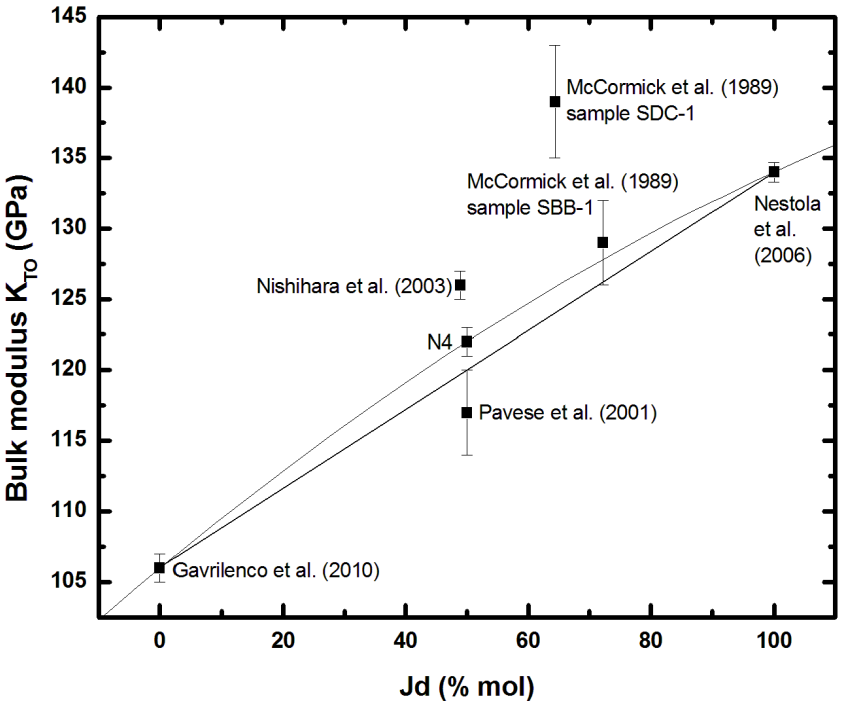

Figure 6. Evolution of K_{T0} as a function of composition along the diopside-jadeite join.

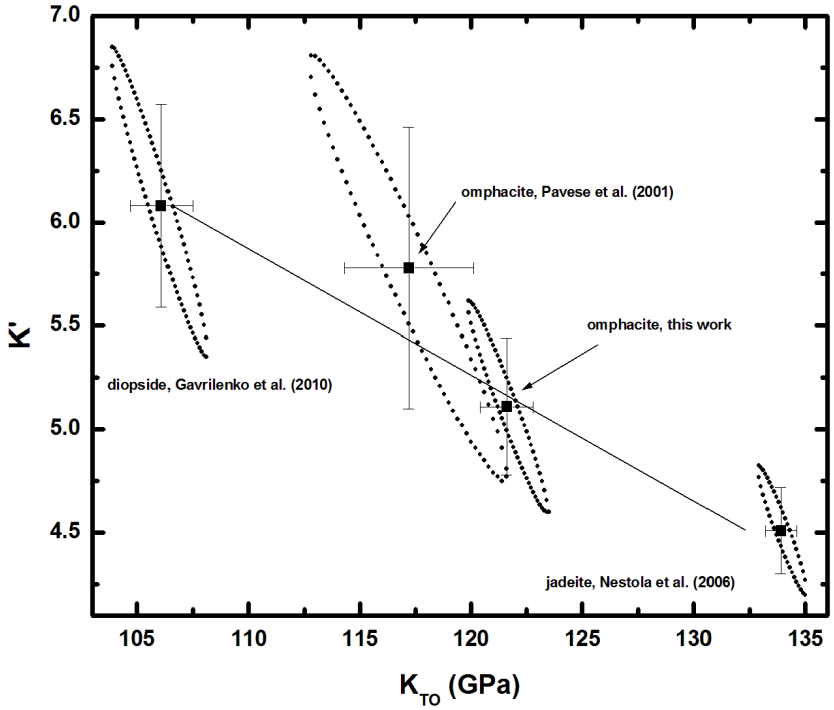

Figure 7. Confidence ellipse for the equation of state of the sample studied in this work and for other samples studied along the diopside-jadeite join.

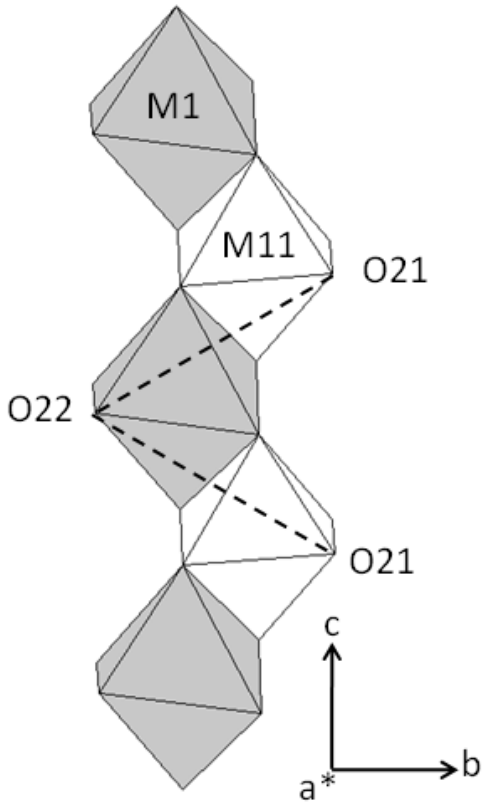

Figure 8. Part of the crystal-structure of the sample studied in this work viewed along the [100] direction. The octahedral M1 and M11 sites are showed. The black line corresponds to the O21-O22-O21 angle.